IV. Spacecraft Control

GUIDANCE AND CONTROL DIVISION

A. Advanced Horizon Scan Platform, *H. H. Horiuchi*

1. Introduction

The horizon scanner, mounted on the servo-controlled platform of a spacecraft, senses the local vertical of the target planet in view. The angle between the optical axis of the platform and the local vertical constitutes an error signal to rotate the platform toward the local vertical.

The scan platform consists of a planet sensor, actuator electronics, a gear train and the spacecraft dynamics (Fig. 1). The spacecraft dynamics includes the effect of platform supporting boom and the motor mounting structure. The content of this study includes a survey of basic performance requirements, system analysis, computer simulation, breadboard design and testing. The advanced planet sensor is being developed, and should be available in fiscal 1968. The planet sensor was simulated with analog circuits.

2. Survey of System Requirements

The basic system requirements have been summarized below from the past advanced studies, the technical reports, and the requirements for the current project. The following specifications have been assumed:

(1) The minimum slewing rate of the platform is 1 deg/sec.

(2) The platform tracks the local vertical of the target planet with an accuracy of ±0.5 deg.

(3) The platform follows the velocity input up to 0.2 deg/sec.

(4) The planet angular diameter varies from 4 to 60 deg.

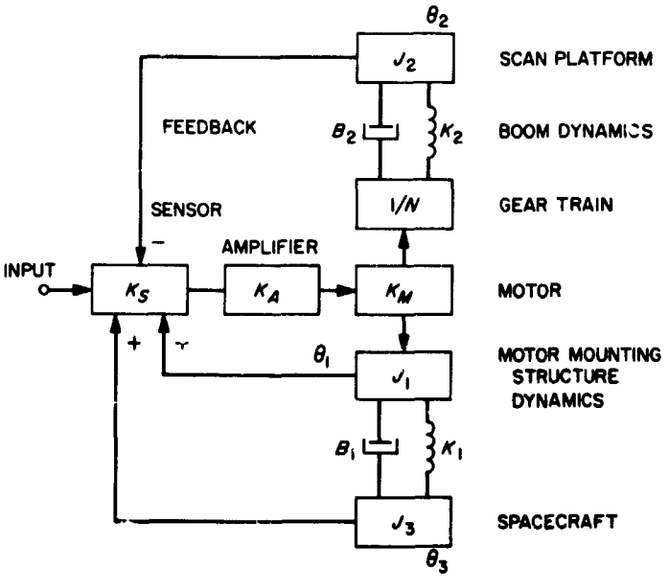

Fig. 1. Scan platform system block diagram

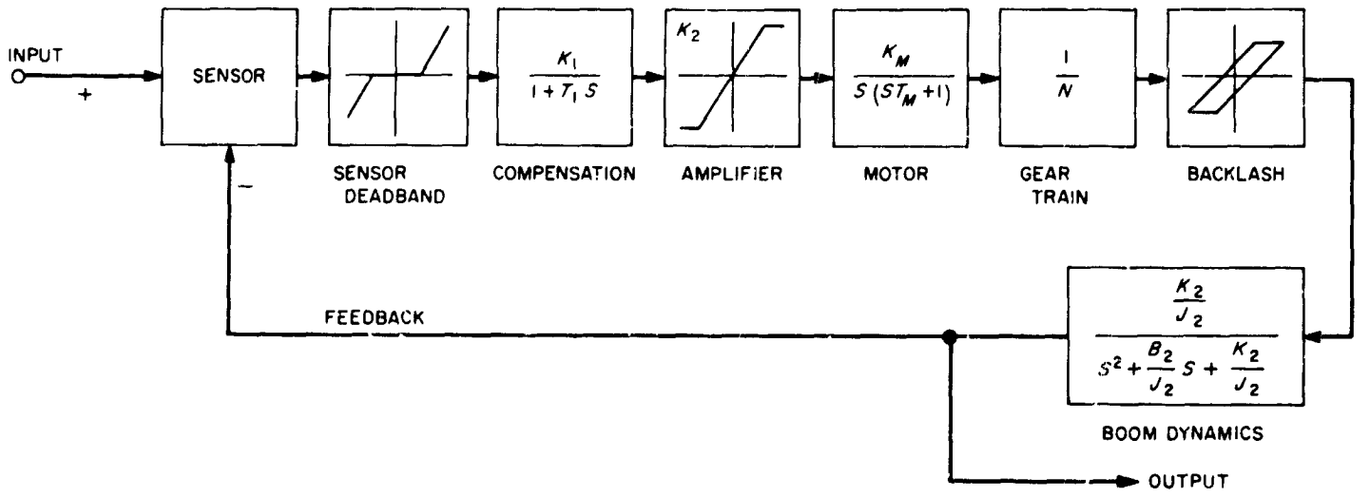

Fig. 2. Platform functional block diagram

(5) The platform jitter is below 500 μrad in track modes of operation.

3. System Description

The system functional block diagram is shown in Fig. 2. The planet sensor is shown as the summing point of the feedback system. The pulse-width modulated error signal from the sensor is integrated, amplified and drives the servo system. The boom structural dynamics is shown as a second-order resonance in the feedback loop.

The sensor consists of two halves of semicircular scanning device, each of which has a view angle of 60 deg, and is made of discrete thermopile elements. The maximum sensor resolution then is determined by the angular separation between the two consecutive elements. As an electronic sweep scans each element at 10 cps, the illuminated element (planet in view) produces a pulse.

The first pulse produced in each sweep closes a summing gate, which in turn produces a step output. This step output remains constant until the end of each sweep.

The step outputs from the two sensors are summed in the summing amplifier to produce a pulse whose width is proportional to the difference between the two step outputs. Hence the pulse width is proportional to the error angle between the platform and the planet local vertical.

The sensor design approach with the discrete thermopile elements seems to provide several advantages over the linear optical sensors. With this approach, the sensor gain may be kept constant over the wide range of input light intensity and also virtually eliminates the thermal drift from the sensor.

4. System Analysis

The Bode diagram of the system shows two structural resonances (Fig. 3). The lower frequency resonance (15 rad/sec, damping factor of 0.07) represents the boom dynamics, and the higher frequency resonance (94 rad/sec, damping factor of 0.01) represents the motor base structural dynamics.

The preliminary system stability analysis was performed using a modified Bode diagram in which the normal loop gain was adjusted to accommodate the gain

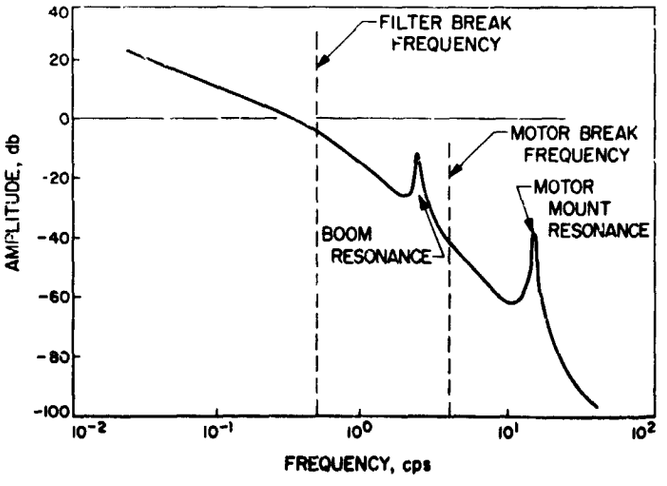

Fig. 3. Scan platform system Bode plot

variation as a function of signal level. The motor break frequency was approximately 4 cps, and the filter break frequency was set for 0.5 cps.

a. Initial simulation. The control system shown in Fig. 2 was simulated for dynamic response using the DSL-90 program on the IBM 7094 digital computer. In this simulation, stiction was not included assuming that the motor delivers sufficient torque to the load.

A permissible range of backlash was investigated to meet the noise requirements. The effect of the backlash to the system noise is summarized in Table 1. The noise level is proportional to the amount of backlash introduced in the range of backlash considered, and the frequency of oscillation is the boom resonant frequency.

Table 1. Effect of backlash to scan system noise

Backlash, rad	±0.0087	±0.0017	±0.00017	±0.000017
Noise, rad	±0.02	±0.004	±0.00035	±0.00004
Noise frequency, rad/sec	15	15	15	15

The tracking capability of the system was investigated by applying a ramp input of 0.0034 rad/sec. The system responds to the ramp input with the average error of 0.0024 rad and with the maximum oscillating amplitude of ±100 μrad. The frequency of oscillation is the boom resonant frequency.

b. System analysis with structural dynamics. The structural dynamics was included in the scan platform control system simulation. The modified section is shown in Fig. 4. The stiction, rolling friction, and backlash are also included in the diagram. The boom dynamics block is placed in series with the feedback loop, while the base dynamics block is placed in parallel with the loop.

The structural dynamics was investigated by using a model which consists of three inertial wheels constrained by springs and dash pots (Fig. 1). The transfer functions of the dynamics blocks were found as follows:

Boom dynamics transfer function.

$$\frac{\theta_2}{T} = \left(\frac{\alpha_1 S + \alpha_0}{S^2 + \beta_1 S + \beta_0}\right)\frac{1}{S^2}$$

Base dynamics transfer function.

$$\frac{\theta_1}{T} = \left(\frac{S^2 + \gamma_1 S + \gamma_0}{S^2 + \delta_1 S + \delta_0}\right)\frac{1}{S^2}$$

and T is the applied torque. The values of the constants, i.e., the α's, β's, γ's and δ's, are determined by the J's, K's and B's in the diagram. Because of a comparatively large assumed inertia of the spacecraft (170 slug-ft²), the effect of the spacecraft motion was neglected in the analysis.

By using the RTL-90 program on the IBM 7094 digital computer, the system root-locus plots were obtained to study the transient and stability characteristics of the system.

5. System Test

a. Initial breadboard test. The primary purpose of this breadboard test was to determine the maximum jitter rate during the slew and null mode when the control system is driven by a pulse-width modulated error signal. The test circuit is shown in Fig. 5. It was found that the tachometer feedback alone was not sufficient to smooth out the input pulses through the motor due to a relatively small motor time constant.

A filter stage was provided for this purpose. The jitter amplitude referred to the platform was approximately ±160 μrad/sec at the motor threshold voltage. This indicated that it might be possible to achieve a low jitter operation using pulsewidth modulation.

b. Transient test on the breadboard. The characteristics of the planet sensor were simulated using analog circuits as shown in Fig. 6. The planet sensor consists of a sawtooth generator, two Schmitt triggers and a summing amplifier.

The error signal is generated by manually rotating the potentiometer shaft for a desired error angle. The unbalance in the potentiometer position causes the Schmitt triggers to trigger at a different input voltage level, thus generating the error signal. The servo loop will move the potentiometer shaft back to its original position. The sensor characteristics as a function of potentiometer position are shown in Fig. 7. In this model, the sensor gain is approximately 10 V/deg within ±1 deg range from the null. The transient error response of the system was observed at test point TP-1. The boom structural resonance was simulated by a second-order resonant circuit. The general patterns of the transient response are shown in Fig. 8.

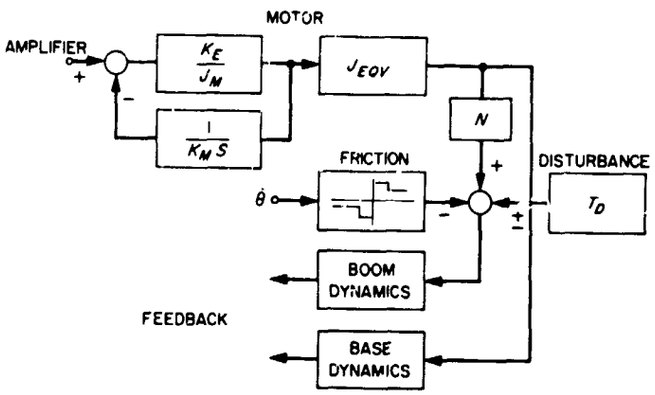

Fig. 4. Scan platform model with dynamics

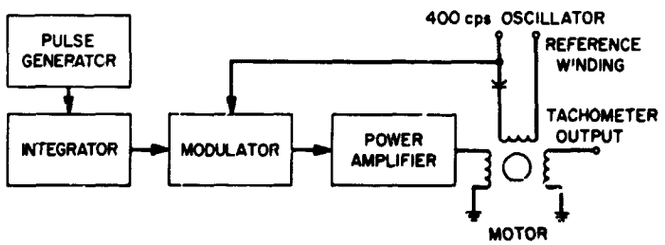

Fig. 5. Pulsewidth modulation test circuit

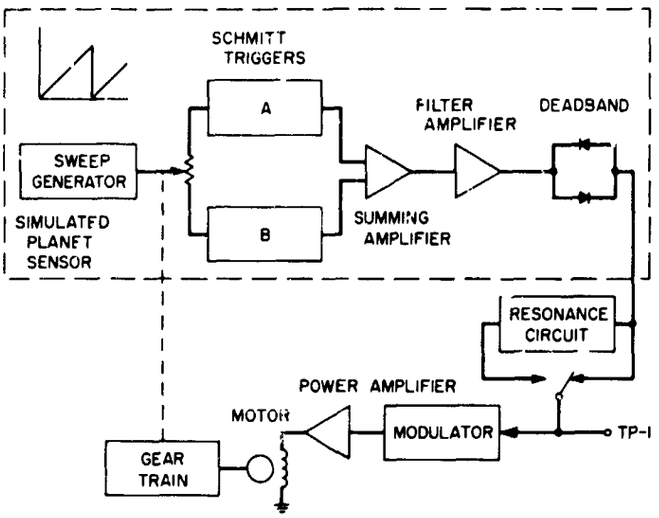

Fig. 6. Scan platform system simulation

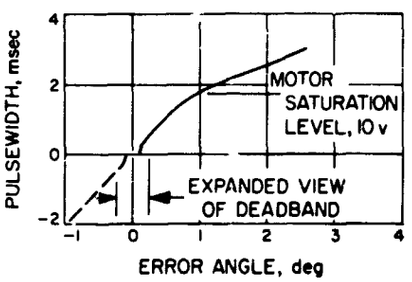

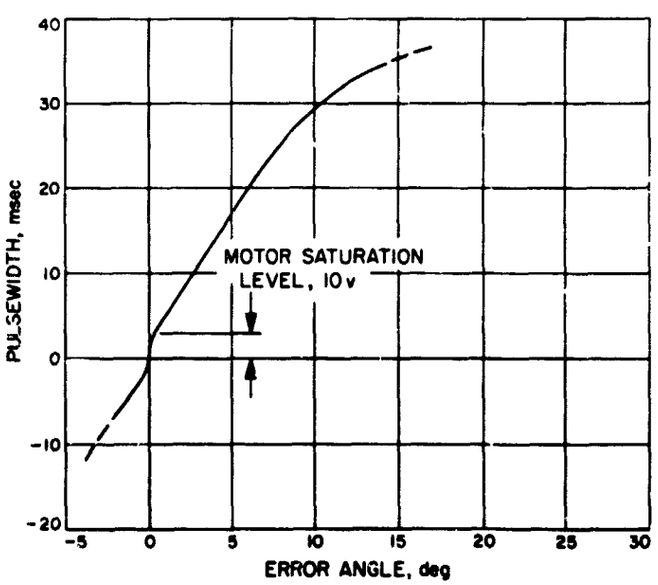

Fig. 7. Characteristics of simulated planet sensor

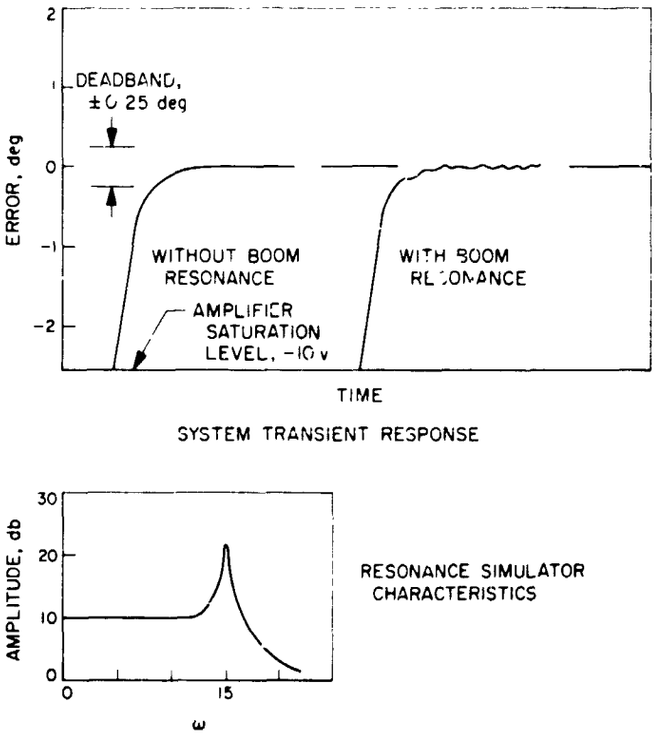

Fig. 8. Platform breadboard test results

The major source of error (other than stiction) in pointing accuracy comes from the planet sensor itself. The selected deadband of ±0.25 deg corresponds to ±2.5 volts at the input to the servo-amplifier. Therefore, all drift and offset voltages referred to the amplifier input (±8.5 mv maximum) becomes negligible. The circuit design was considerably simplified by using integrated circuit amplifiers.

B. Calibration Procedure Used in the Attitude Control Nozzle Thrust Measuring Technique,

J. D. Ferrara

The intent of this report is to update a previous report entitled "Attitude Control Thrust-Nozzle Measuring Techniques" by J. C. Randall (SPS 37-39, Vol. IV, pp. 40–42). The cantilever beam and strain gage approach, as detailed in Randall's report, has been attempted. A flattened rod immersed in a pool of mercury has been added behind the valve nozzle combination in order that the amount of damping in the system can be easily varied (see Fig. 9). In using the strain gage approach, considerable damping is required to measure steady-state thrust levels; a minimum amount of damping is required in determining the impulse bit as outlined in Randall's report.

Fig. 9. Micrometer mounted in front of thrust nozzle

The strain gage approach presented the following three problems:

(1) The gages were found to be very sensitive to 60-cycle noise and vibrations from the mechanical pump used in the vacuum station.

(2) The gages were found to be sensitive to various temperature and pressure changes in and out of the vacuum jar which resulted in a zero shift, making any calibration procedure difficult.

(3) The gages were found to be slightly sensitive to the flow of nitrogen gas in the cantilever beam feed tube.

Because of the problems encountered with the strain gages, a photoelectric pickoff was installed. A square-edged plate was mounted to the thruster body such that motion of the beam results in a varying amount of light passing through a slot immediately above the photosensitive cell. This technique appears to work very well and is insensitive to the problems encountered with the strain gage. The photoelectric pickoff that is currently being used, however, is not shown in either Figs. 9 or 10.

We are presently calibrating the system using the following method: By mounting a micrometer to the frame immediately in front of the nozzle cone (see Fig. 9) and by advancing the micrometer in known increments and recording the voltage output of the photocell, a curve of thruster displacement versus output voltage can be generated. A stainless steel ball is then suspended in front of the nozzle from a micrometer attachment. This is shown in Figs. 10, 11. If then the micrometer is moved a distance X_m, the beam, in equilibrium with the applied force, will

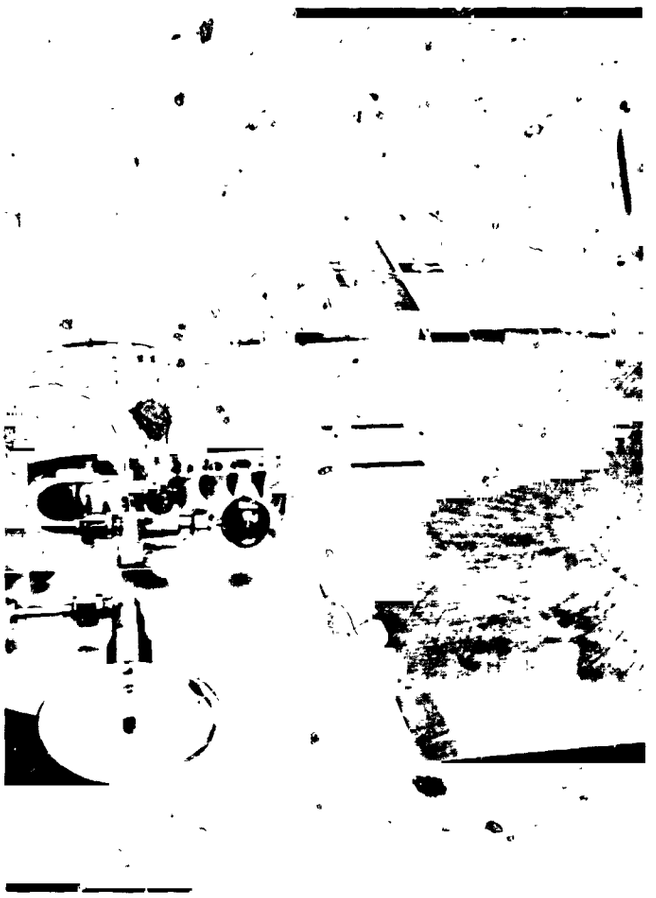

Fig. 10. Steel ball suspended in front of thrust nozzle

deflect an amount X_b; X_b is determined from the voltage output versus thruster displacement curve described above. A study of Fig. 11 indicates that:

$$f = (m)(\tan\theta) = \frac{(m)(x)}{(l^2 - x^2)^{1/2}} \qquad (1)$$

m = weight of ball, gm

$x = |X_m - X_b|$, in.

l = length of wire plus one-half the diameter of the ball, in.

f = applied force, gm.

Since l is from 2 to 3 in. and x is on the order of 0.001 to 0.003 in., f can be accurately determined by a simplification of Eq. (1):

$$f = \frac{(m)(x)}{(l)} \qquad (2)$$

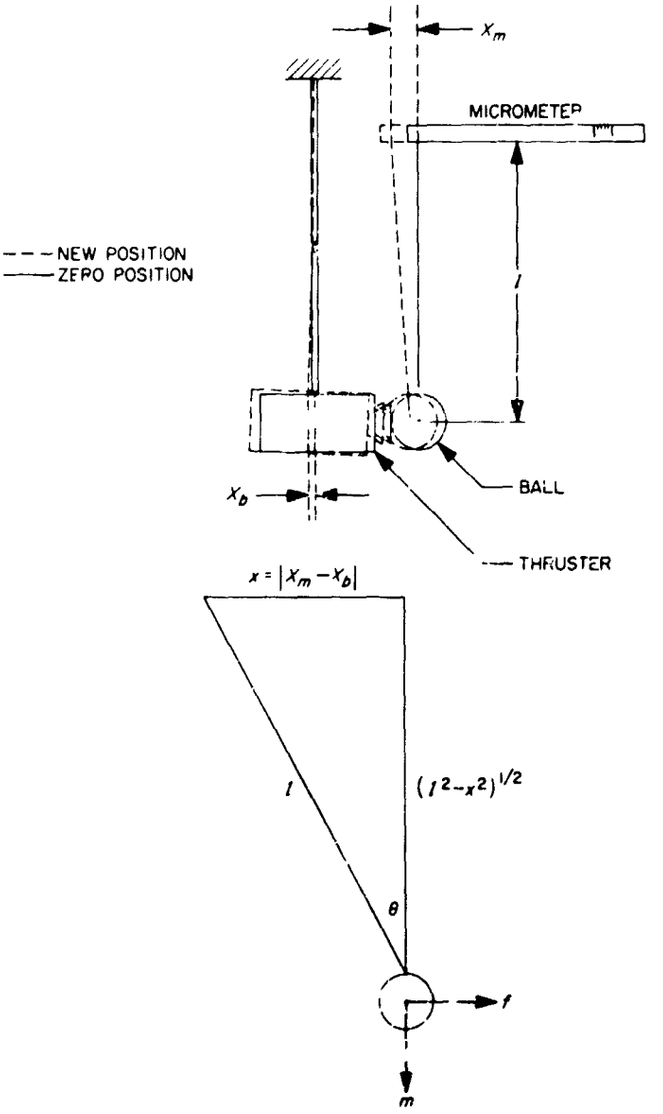

Fig. 11. Beam displacement calibration procedure for measuring nozzle thrust

Using Eq. (2) and the curve mentioned above, a curve can be plotted of the photocell voltage output versus the applied force (f), which is equivalent to the force produced by a firing of the thruster. With this method, the thrust level can be very accurately determined. The impulse bit is determined as outlined in Randall's report (SPS 37-39, Vol. IV, pp. 40–42).

When this calibration procedure is perfected, a test program will begin using *Mariner* type thrusters to verify the results of a computer program described in the SPS report, "Parametric Analysis for Steady-State Performance of Attitude Control Thrusters," by J. D. Ferrera and P. M. McKown (SPS 37-42, Vol. IV, pp. 47–48).

C. Generalized Cruise Gas Requirement Study,

G. Paine

1. Introduction

The aim of this study is to provide an estimate of the cruise gas requirement for a general spacecraft as a function of spacecraft weight. If a better estimate is required, then the craft configuration must be specified since cruise gas consumption depends heavily on both the spacecraft weight and configuration. This study can be used in an evaluation of the tradeoffs between various gas systems as well as of the tradeoffs between communication rates and powers and antenna pointing accuracy.

The general spacecraft chosen has a cylindrical geometry (Fig. 12), a uniform mass density, and no solar panels The addition of solar panels can be allowed for easily; however, their addition at this stage complicates the design unnecessarily as their size depends on the power requirements and the mission trajectory.

There are several types of gas attitude control systems that can be considered: cold gas, warmed gas, and hot gas. The use of a dual thrust level system can save considerable gas in a large spacecraft by providing a low I_{sp} during cruise and a high I_{sp} during spacecraft maneuvers. The use of heaters in a cold gas system fulfills these requirements as the heaters may be turned on for spacecraft maneuvers and left off during cruise. Such a system would be relatively simple and fail-safe.

The attitude control system analyzed is a cold gas system in which the jets are sized for some angular acceleration constant. The constant is determined by the maximum allowable initial acquisition time and the midcourse maneuver times. A dual level system was not analyzed as they are not employed on current interplanetary spacecraft. Likewise the minimum on-time for a jet was held at current levels, rather than being reduced to lower the cruise gas requirements in a large spacecraft.

The disturbance torques acting on the spacecraft have been lumped into two classes: In the first are those resulting from valve leakage. The second includes all other sources, such as unbalanced solar pressure and gravity gradients. The second must be estimated for any particular spacecraft configuration and mission.

2. Conclusions

The cruise gas consumption for a 200-day mission is displayed in Fig. 13. These results include triple redundancy but no tankage factor. The parameters not appearing on the figure are from *Mariner IV*. The results can be scaled directly for missions lasting other than 200 days. The curve for zero disturbance torque limit cycle gas consumption can be scaled inversely to the limit cycle deadband. Less gas would be required with the addition of solar panels and with the attitude control jets located at their extremities since both the constant disturbance torque and the zero disturbance torque gas consumptions are inversely proportional to the jet lever arm.

It is apparent that for the spacecraft geometry and other parameters assumed that cruise gas consumption

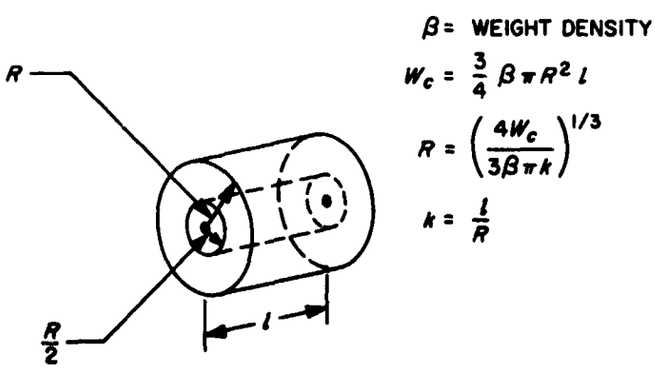

Fig. 12. Spacecraft whose configuration is a hollow cylinder

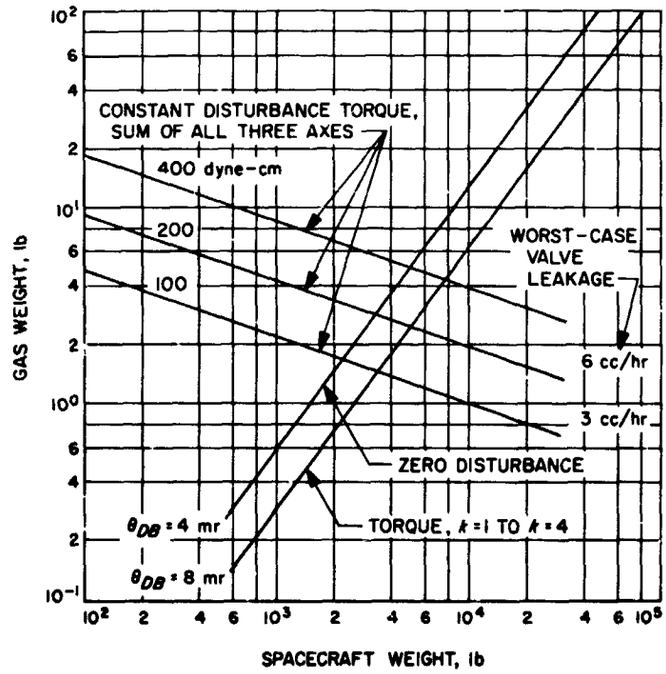

Fig. 13. Cruise gas consumption during 200-day mission

depends more on disturbance torque level than it does on the zero disturbance torque situation for spacecraft weighing less than about 2000 lb.

If the non-leakage disturbance torques are unspecified, it is reasonable in the light of the disturbance torques encountered on *Mariners II* and *IV* to allow 2.0 lb of gas for cruise purposes for spacecraft weighing less than 2000 lb. This is equivalent to about a 75 dyne-cm disturbance torque on a 500-lb craft without solar panels or about 225 dyne-cm on a 500-lb craft with them. On a 200-day mission, an additional 0.75 lb of gas will cover the worst-case valve leakage.

For missions where either the spacecraft is heavy or where the disturbance torques are expected to be small, the zero disturbance torque gas consumption will be the dominating factor and the gas consumption will vary according to spacecraft weight raised to the 4/3 power.

3. Gas Consumption

As the spacecraft studied is not equipped with solar vanes which passively control the spacecraft, the gas consumption will depend directly on the disturbing torque. For a constant disturbing torque, Fig. 14 shows the relationship between the magnitude of the torque and the weight of the gas consumed for a spacecraft which oscillates inside a symmetrical deadband.

To the left of τ_0, the marginal torque in Fig. 14, the spacecraft oscillates and touches both sides of the deadband. To the right, the spacecraft touches only one side of the deadband.

If the maximum (worst-case) disturbance torque allowed is greater than τ_1, then the gas consumption is determined totally by the disturbance torque and the mission duration. If the maximum disturbance torque is less than τ_1, then the maximum gas consumption will occur with no disturbance torque present, and the gas consumption depends on a variety of vehicle parameters.

4. Disturbance Torques

A number of disturbances act on the spacecraft. They include externally caused torques such as those arising from solar pressure and gravity as well as internally generated ones from valve and piping gas leakage, as well as other sources.

Each disturbance torque can be related to a wide range of parameters. Here the parameters which depend on vehicle weight are called out explicitly while the others are held constant. So, for instance, the solar torques will be taken as proportional to vehicle area, or vehicle weight raised to the 2/3 power, neglecting the many other factors influencing solar torques. Valve leakage, which can produce a torque is taken as a worst-case constant, even though it varies from valve firing to valve firing. The same gas consumption will arise whether all twelve valves are leaking or whether only six are leaking and the other six must be fired to produce a restoring torque.

The gas weights required to counterbalance each of these is shown in Fig. 15. The constant disturbing torque

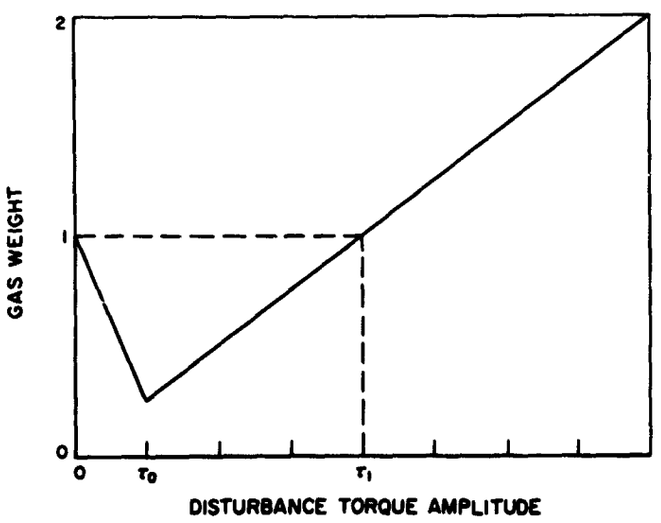

Fig. 14. Mass of consumed gas versus disturbance torques

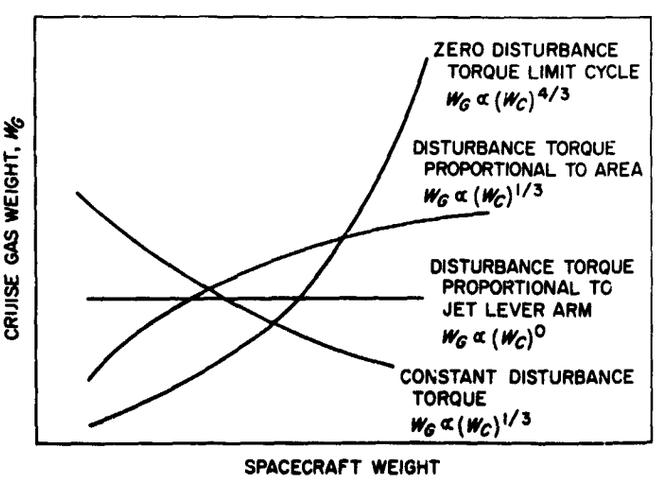

Fig. 15. Cruise gas consumption versus spacecraft weight and disturbance torque type

and the special case of zero disturbing torque gas consumptions are also included. In each case the counterbalancing torque is proportional to the lever arm, or spacecraft weight raised to the 1/3 power. Thus in the example of an area-dependent torque, the gas required increases only as the 1/3 power of the spacecraft weight although the disturbance increases by the 2/3 power.

From Fig. 15 it can be seen that there are two distinct regions: one where the disturbance torques control the gas consumption, and another where the zero disturbance torque gas consumption dominates. The weight of the gas required depends in the former region on the predominant disturbance and will vary with spacecraft weight according to the nature of the largest disturbance. In the former region, the worst worst-case valve leakage gas consumption adds directly to the other gas weights.

5. Mathematics of Gas Consumption

As has been shown in many other places (Refs. 1, 3 and 4)[1] the weight of the gas consumed depends on several simple formulae,—making no allowances for either the triple gas redundancy or tankage weight factors. The formulae below give the gas consumption for each axis: The terminology is listed in Table 2.

a. Zero disturbance torque gas consumption:

$$W_G = \frac{I(\alpha\Delta t)^2 t_m}{4LI_{sp}\vartheta_{DB}}$$

b. Marginal disturbance torque gas consumption: Marginal torque is the smallest torque for which the attitude control system touches only one side of the deadband.

$$W_G = \frac{I(\alpha\Delta t)^2 t_m}{16LI_{sp}\theta_{DB}}$$

$$\tau_0 = \frac{(\alpha\Delta t)^2 I}{16\theta_{DB}}$$

c. Torque balance gas consumption:

$$W_G = \frac{t_m \tau_D}{LI_{sp}}$$

d. Largest disturbance torque with gas consumption equal to zero disturbance torque gas consumption:

$$\tau_1 = \frac{(\alpha\Delta t)^2 I}{4\theta_{DB}}$$

[1]Also by H. K. Bouvier: *A Field Guide to Limit Cycles*, and *Mariner IV Disturbance Torques*, JPL-IOM 344-543.

Table 2. Nomenclature

W_G	gas weight
I	moment of inertia of spacecraft
L	gas jet lever arm
α	acceleration constant
Δt	minimum on time
t_m	mission time
I_{sp}	specific impulse
θ_{DB}	deadband
τ_0	marginal torque
τ_1	unbalance torque resulting in the same gas consumption as no disturbing torque
β	spacecraft weight density
k	spacecraft length to radius ratio
g	gravity
W_c	spacecraft weight
R	spacecraft radius
l	spacecraft length
τ_D	disturbance torque

6. General Spacecraft Configuration

The general spacecraft was chosen to be a hollow cylinder (Fig. 12) with a uniform mass density. The gas jets are placed so that the roll jets have a lever arm (L) equal to the radius (R), and the pitch and yaw jets so that they have a lever arm equal to the greater of the radius (R) or half the vehicle length (l). In the following functions, k is the ratio of spacecraft length to radius, and I is the inertia.

a. Pitch and yaw axis functions.

For all k

$$I = \frac{4W_c}{3g}\left(\frac{R^2}{4} + \frac{l^2}{12}\right) - \frac{W_c}{3g}\left(\frac{R^2}{16} + \frac{l^2}{12}\right)$$

or

$$I = \frac{W_c}{4g}\left(\frac{4W_c}{3\beta\pi k}\right)^{2/3}\left(\frac{5}{4} + \frac{k^2}{3}\right)$$

For $k \leq 2$, $L = R$, and

$$\frac{I}{L} = \frac{3\beta k\pi}{16g}\left(\frac{4W_c}{3\beta k\pi}\right)^{4/3}\left(\frac{5}{4}+\frac{k^2}{3}\right) = \frac{W_c R}{4g}\left(\frac{5}{4}+\frac{k^2}{3}\right)$$

For $k > 2$, $L = l/2$, and

$$\frac{I}{L} = \frac{3\beta\pi}{8g}\left(\frac{4W_c}{3\beta k\pi}\right)^{4/3}\left(\frac{5}{4}+\frac{k^2}{3}\right) = \frac{W_c R}{2kg}\left(\frac{5}{4}+\frac{k^2}{3}\right)$$

b. Roll axis function.

$$I = \frac{2W_c R^2}{3g} - \frac{W_c R^2}{24g} = \frac{5W_c R^2}{8g}$$

For any k, $L = R$, and

$$\frac{I}{L} = \frac{15\beta k\pi}{32g}\left(\frac{4W_c}{3\beta k\pi}\right)^{4/3} = \frac{5W_c R}{8g}$$

These factors, which enter directly into the zero disturbance torque gas consumption, are plotted in Fig. 16 for some typical parameters: $k = 1$ and $\beta = 15$ lb/ft.[3] On Fig. 16, the actual (I/L) values are plotted for *Mariner IV* and for a proposed Venus-Mercury 1973 craft. The differences are explained by the solar panels on these two craft. While the solar panels increase the inertia per unit spacecraft weight significantly, they increase the jet moment arm even more rapidly, giving rise to a net reduction in I/L.

7. Gas Weights and Results

Even with the concepts stated earlier, more assumptions are necessary before the gas requirements can be set down explicitly. Some of these concern the vehicle geometry, others concern the jet size and minimum on-time, while still others relate the disturbances and deadbands of the three axes.

The gas weight shown is for three-axes stabilization and includes the triple redundancy factor but does not allow for tankage. The gas weights should be multiplied by 2.6 to obtain gas weight plus variable tankage weight.

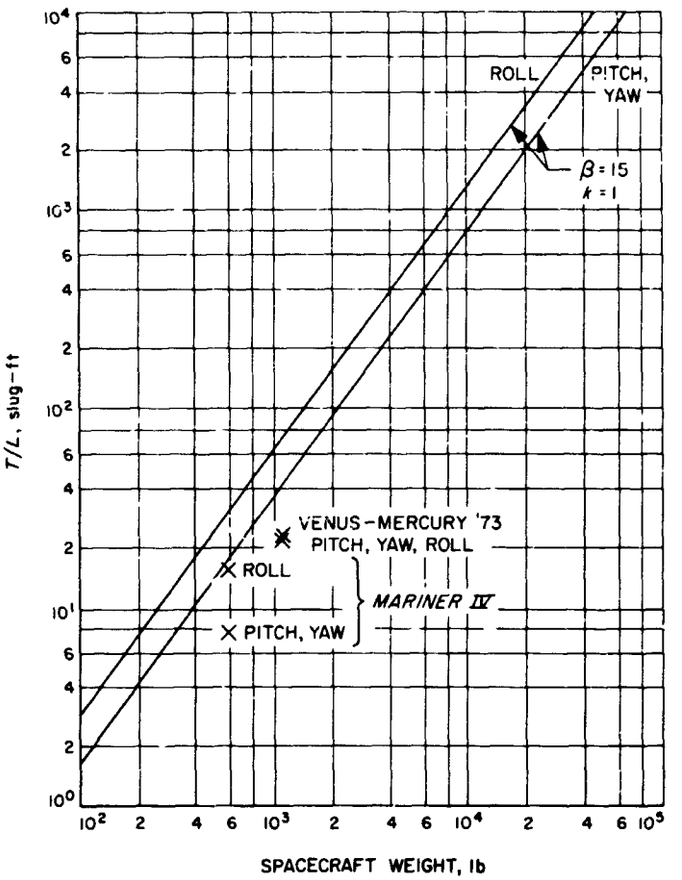

Fig. 16. Ratio of inertia to lever arm length versus spacecraft weight

The gas weight factor to account for half-system performance is 1.5 rather than 3 in the case of valve leakage.

In Fig. 13, gas consumption is shown as a function of spacecraft weight for $k = 1$ to $k = 4$, three levels of constant disturbance torque, two levels of gas leakage, and two deadband widths.

In Fig. 13 the following additional constants, taken from *Mariner IV* (see Ref. 4), are assumed:

θ_{DB} = same for all three axes

$\alpha = 0.45$ mr/sec^2

$\Delta t = 0.02$ sec

$I_{sp} = 60$ sec

$t_m = 200$ days

$\beta = 15$ lb/ft^3

References

1. Project Report 4290, Barnes Engineering Co., 1966.
2. Nicklas, J. C., and Vivian, H. C., *Derived-Rate Increment Stabilization,* TR 32-69, Jet Propulsion Laboratory, Pasadena, Calif., July 31, 1961.
3. Turk, W., *Ranger Block III Attitude Control System,* TR 32-663, Jet Propulsion Laboratory, Pasadena, Calif., Nov. 15, 1964.
4. *Mariner-Mars 1964 Project Report: Mission and Spacecraft Development.* Vol. I, TR 32-740, Jet Propulsion Laboratory, Pasadena, Calif., Mar. 1, 1965.